ACS APPLIED MATERIALS & INTERFACES

Research Article

Cite This: ACS Appl. Mater. Interfaces 2018, 10, 12639−12650

www.acsami.org

Interface Engineering and its Effect on WO_3-Based Photoanode and Tandem Cell

Yang Liu,[†,‡] Bryan R. Wygant,[‡] Oluwaniyi Mabayoje,[‡] Jie Lin,[‡,§] Kenta Kawashima,[‡] Jun-Hyuk Kim,[‡] Wenzhang Li,[†] Jie Li,[*,†] and C. Buddie Mullins[*,‡]

[†]College of Chemistry and Chemical Engineering, Central South University, Changsha 410083, China

[‡]Department of Chemical Engineering and Department of Chemistry, University of Texas at Austin, Austin, Texas 78712-0231, United States

[§]Pen-Tung Sah Micro-Nano Science and Technology Institute, Xiamen University, Xiamen, Fujian 361005, China

Supporting Information

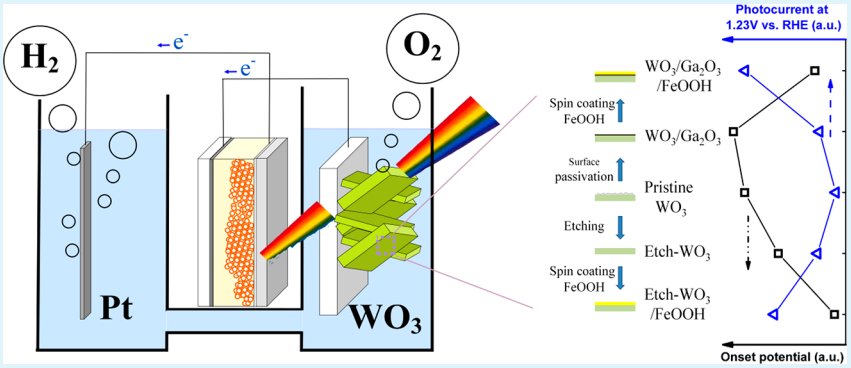

ABSTRACT: During photoelectrochemical (PEC) water splitting, the reactions occur on the surface of the photoelectrode. Therefore, the properties of the interfaces between the various components of the electrode (semiconductor/semiconductor, semiconductor/catalyst, or photoelectrode/electrolyte) affect the PEC performance of the composite material. Notably, surface trap states may hinder charge transfer and transport properties, and also cause Fermi pinning, affecting the quasi-Fermi level and onset potential under illumination, which may in turn influence the PEC performance of the corresponding tandem cells. In this study, plate-like WO_3 array films prepared by an aqueous chemical growth method were employed to highlight the effect of interfacial properties on the performance of a WO_3-based photoanode. The Mott−Schottky and linear sweep voltammetry experiments prove the existence of surface trap states and Fermi pinning for pristine WO_3, which are alleviated after an "etching" treatment and disappeared after surface passivation by a Ga_2O_3 layer. Both etching and passivation increase the oxygen evolution activity and the Faradaic efficiency for the oxygen evolution reaction (OER). After loading a permeable catalyst (FeOOH), the photocurrent is further increased, and there is a synergistic effect between loading of the electrocatalyst with etching or passivation. The onset potentials of the samples follow the trends: etch-WO_3/FeOOH < WO_3/FeOOH ≤ WO_3/Ga_2O_3/FeOOH < etch-WO_3 < WO_3 < WO_3/Ga_2O_3, indicating that the interfacial properties have a significant effect on the PEC performance. Meanwhile, the modified WO_3-based electrode was combined with a dye-sensitized solar cell to fabricate tandem cell, which showed 2.42-fold photocurrent density compared with the pristine WO_3-based tandem cell.

KEYWORDS: *WO_3, surface states, etching, passivation, tandem cell, solar water splitting*

1. INTRODUCTION

Since 1972, photocatalytic or photoelectrochemical (PEC) water splitting for producing hydrogen and oxygen has been a hot subject of intense research,[1] and numerous materials[2−4] have been discovered and reported as photoelectrodes. However, the band position of most materials make them unsuitable to satisfy H_2 and O_2 evolution together, and additional applied potential is needed to perform water splitting.

In recent years, tandem cells have been reported for water splitting without additional applied potential. $NiFeO_x$-modified hematite was combined with a TiO_2/Pt loaded amorphous silicon photocathode in 0.5 M phosphate solution (pH 11.8),[5] and the output photocurrent was about 0.7 mA/cm^2. The solar-to-hydrogen conversion efficiency was 3.1% when a WO_3 photoanode was used in a tandem unassisted PEC water splitting system with a TiO_2-based dye-sensitized solar cell (DSSC), and increased to 5.7% when a $BiVO_4$-sensitized

Received: January 6, 2018
Accepted: April 2, 2018
Published: April 2, 2018

DOI: 10.1021/acsami.8b00304
ACS Appl. Mater. Interfaces 2018, 10, 12639−12650

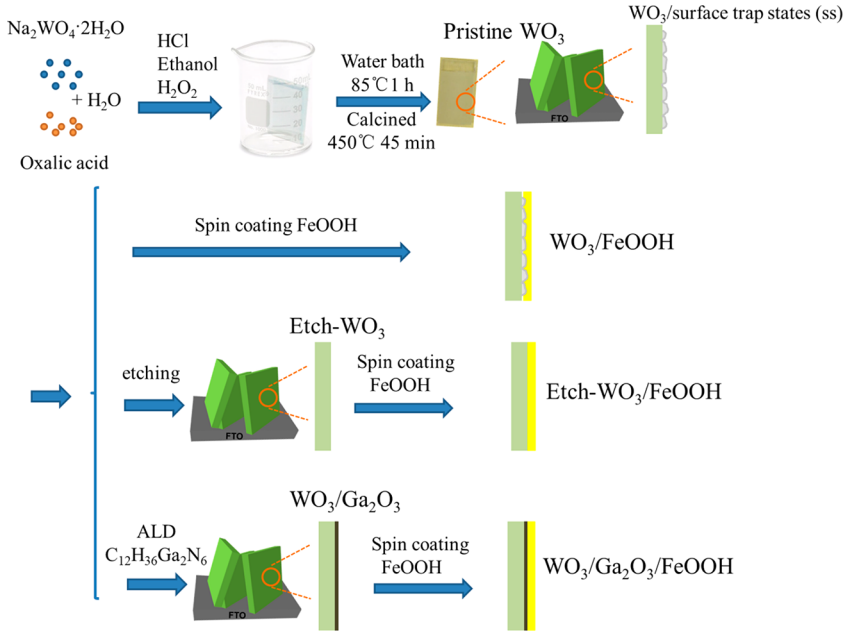

Figure 1. Schematic illustrations of synthesis of WO_3 and the surface-modified samples.

mesoporous WO_3 film was combined with a porphyrin-DSSC with a high voltage open circuit potential (V_{OC}).[6,7] Considering the light absorption balance between the photoanode and solar cell (or photocathode), a WO_3-based photoanode is an ideal candidate due to its reasonable bandgap (E_g = 2.6−2.8 eV), great hole mobility (10 cm^2 V^{-1} s^{-1}) and moderate hole diffusion length (150 nm).[8,9] Despite this, the match between WO_3 photoanodes and solar cells in tandem unassisted PEC water splitting systems is not good. This is because the WO_3 photoanode cannot match the V_{OC} of the solar cell as well as the low current densities from the photoanode at the potential provided by the solar cell.

To achieve unassisted water splitting with high efficiency, one possible strategy is to increase the V_{OC} with dual or multiple junction configuration solar cells (such as double-junction Si,[10] GaAs/InGaAsP[11]), which can compensate for the large overpotential of the oxygen evolution reaction (OER), further increasing the current density of the photoanode to approach the theoretically possible photocurrent value.[12] Another possibility for gaining a good match is decreasing the onset potential or increasing the photocurrent in the low applied potential region of the photoanode. The onset potential (V_{OP}) of a photoanode can be calculated by the formula ($V = F_{re} - \Phi_{ph} + \eta$), where F_{re}, Φ_{ph}, and η are the electrochemical potential of the solution, photovoltage and kinetic overpotential, respectively. In reality, the onset potential is also dependent on interface phenomena, which are associated with some possible factors, including surface termination, surface catalysis, Fermi level position and surface traps.[13−15] Among them, surface traps may result in increasing the stored charge,[16] surface recombination[17] and pinning of the Fermi level.[18] In such a manner, the compositional and electronic properties of the semiconductor surface are not in the ideal situation, which may influence the value of Φ_{ph} of the photoanode.[19] Etching the surface of the semiconductor is considered as a strategy to decrease the thickness of the surface disordered layer and dissolve surface traps, and can result in a negatively shift of the onset potential as well. Zheng et al. enhanced the low-bias performance of a hematite photoanode by flame-doping, oxalic acid etching and surface catalyst modification.[20] A dual etched/reduced WO_3 film was obtained by dipping the WO_3 film in a solution containing poly(vinylpyrrolidone) (PVP) and ascorbic acid.[21] Most recently, a WO_3 film was etched by dipping into thioacetamide solution at 90 °C for 10 h.[22] The modified WO_3 film also shows a negative shift in onset potential and increased photocurrent in the low potential region.

Loading catalysts on the surface of the semiconductor can also decrease the onset potential. It is because the electrocatalyst promotes the water oxidation reaction by decreasing the kinetic overpotential (η).[23] The interface between the original semiconductor and catalyst is critical for photogenerated charge transfer and PEC performance of the integrated photoanode. To get high performance, the catalyst should match well with the semiconductor in band alignment and structure.[24] Two different types of current−potential curves were found with the loading of Co-Pi[25,26] and FeOOH,[27,28] and both an improvement[27] and a decrease[29] of PEC performance can be seen after electrodeposition of the FeOOH under irradiation. Considering the control sample (pristine WO_3) was not treated at a similar potential under irradiation, it is difficult to discuss the influence of the interface without taking the effect of electrochemical treatment and illumination into account. However, the trapping sites on the surface of the original semiconductor will still exist at the interface between semiconductor and catalysts. Because of the charge trapping, the photogenerated holes may recombine with the electrons at the interface instead of being transferred to the catalyst or electrolyte.[30] Thus, surface traps of the semiconductor should be considered before a catalyst can be employed. Meanwhile, most of the non-noble catalysts for the OER suffer from deleterious degradation reactions in the low pH region,[31] and the Faradaic efficiency of water oxidation for WO_3-based materials is low in the low pH region, too.[32] Because WO_3 may be thermodynamically unstable in an electrolyte solution with pH > 4,[33] the stability also needs to be considered during OER measurements.

In addition to protecting the electrode from chemical dissolution and corrosion, surface passivation is also a good

DOI: 10.1021/acsami.8b00304
ACS Appl. Mater. Interfaces 2018, 10, 12639−12650

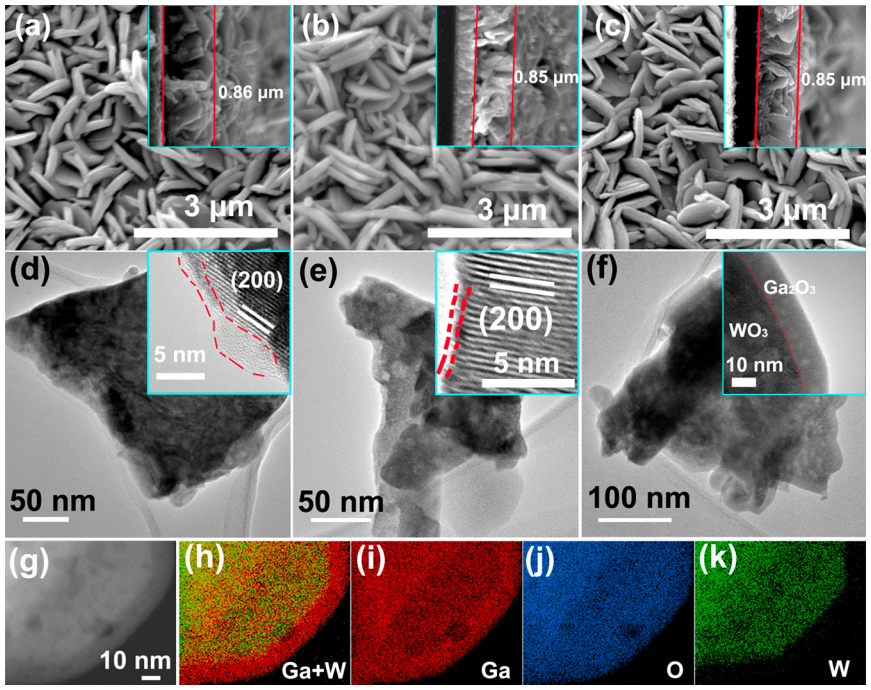

Figure 2. SEM images of (a) bare WO_3, (b) etch-WO_3, (c) WO_3/Ga_2O_3. TEM and HRTEM images of (d) bare WO_3, (e) etch-WO_3, (f) WO_3/Ga_2O_3, (g) STEM image of WO_3/Ga_2O_3, and (h–k) the corresponding EDX elemental mappings.

strategy to impede recombination at the surface states of the semiconductor, which has the possibility to change the onset potential. Choi et al.[34] loaded an alumina overlayer on the surface of a transparent WO_3 particle film by atomic layer deposition (ALD). The modified nanoparticle film showed a slightly positive onset potential compared with the WO_3 film before coating with the passivation layer, which is different from the hematite photoanodes passivated with alumina overlayers.[35] These indicate that passivation may inhibit the recombination of electrons and holes at the surface traps, but the overlayer consists of a new material that may affect the energy level of the photoanode by field effect passivation.[36] The HfO_2 as passivation layer was also used to cover the surface of WO_3 particle film and plate-like arrays film, showing a slightly positive shift of onset potential.[37,38] Consequently, the shift in the onset potential will depend on the individual situation.

The electrochemical properties of the interface are key factors for the onset potential and the PEC performance of the semiconductor. In this study, WO_3 plate-like array films prepared by an aqueous chemical growth method were employed as a research tool to investigate the shift of onset potential and its effect on the PEC performance. We treated the WO_3 film by etching or passivation, and then loaded catalyst by a chemical bath method. To further understand the effect of interface properties and the corresponding onset potential, the tandem cells were also constructed using the as-prepared photoanode and a DSSC, which demonstrates a possibility of activating the tandem cell's water splitting capabilities by modifying the surface of the photoelectrode.

2. RESULTS AND DISCUSSION

2.1. Physical Characterization. Here we use a WO_3 plate-like film as the starting material (see the experimental section in Supporting Information and schematic illustrations of synthesis in Figure 1). The XRD peaks match well with the standard monoclinic WO_3 (PDF 72-0677) and tetragonal SnO_2 (PDF 46-1088), confirming WO_3 is loaded on the FTO (in Figure S1a).[39] After an etching treatment (etch-WO_3) or coating of a Ga_2O_3 passivation layer (WO_3/Ga_2O_3), no obvious changing of peaks is found due to the low loading amount of Ga_2O_3 (Figure S1a and b). In Figure S1c, similar XRD patterns are seen after subsequent loading of electrocatalyst (WO_3/FeOOH and etch-WO_3/FeOOH). In scanning electron microscope (SEM) images (Figures 2a–c and S2), all the samples show a plate-like array morphology, with a film thickness of ~0.86 μm. After depositing FeOOH (Figures S2 and S3), the surface of the WO_3 plates seems to be wrapped by a rough gauze-like material which is likely FeOOH. Energy-dispersive X-ray spectroscopy (EDX) elemental mapping of the WO_3/Ga_2O_3/FeOOH cross-section reveals that Ga_2O_3 and FeOOH have been coated on the WO_3 (Figure S4). X-ray photoelectron spectroscopy (XPS) further confirms the presence of each element derived from the electrocatalyst (FeOOH) and the passivation layer (Ga_2O_3) in Figures S5a–c, 5e, and S7. The ratio of the surface hydroxyl groups and lattice oxygen groups increases after loading of FeOOH (Figure S5b), which may result from the hydroxylated surface of the FeOOH layer.[40] In addition, the atomic ratio of Ga/W on the surface of the WO_3/Ga_2O_3 increases with an increase in the number ALD cycles (Figures S8 and S9 and Table S1).

A comparison between the WO_3 and the etch-WO_3, as well as the WO_3/Ga_2O_3, is also made via transmission electron microscopy (TEM) analysis. The low-resolution TEM images (Figure 2d–f) confirm that the WO_3-based films are composed of plates, which is consistent with the SEM results (Figure 2a–c). The high-resolution TEM (HRTEM) image of WO_3 (inset of Figure 2d) shows a disordered layer (about 1.3 nm) at the edge of the WO_3 plate. After etching, the surface disordered layer (~0.5 nm) becomes thinner as marked (Figure 2e). In the HRTEM and STEM images (Figure 2f and g), a new material covers the bulk WO_3 plate. To determine the identity of this component, we measured the EDX elemental mapping. The

DOI: 10.1021/acsami.8b00304
ACS Appl. Mater. Interfaces 2018, 10, 12639–12650

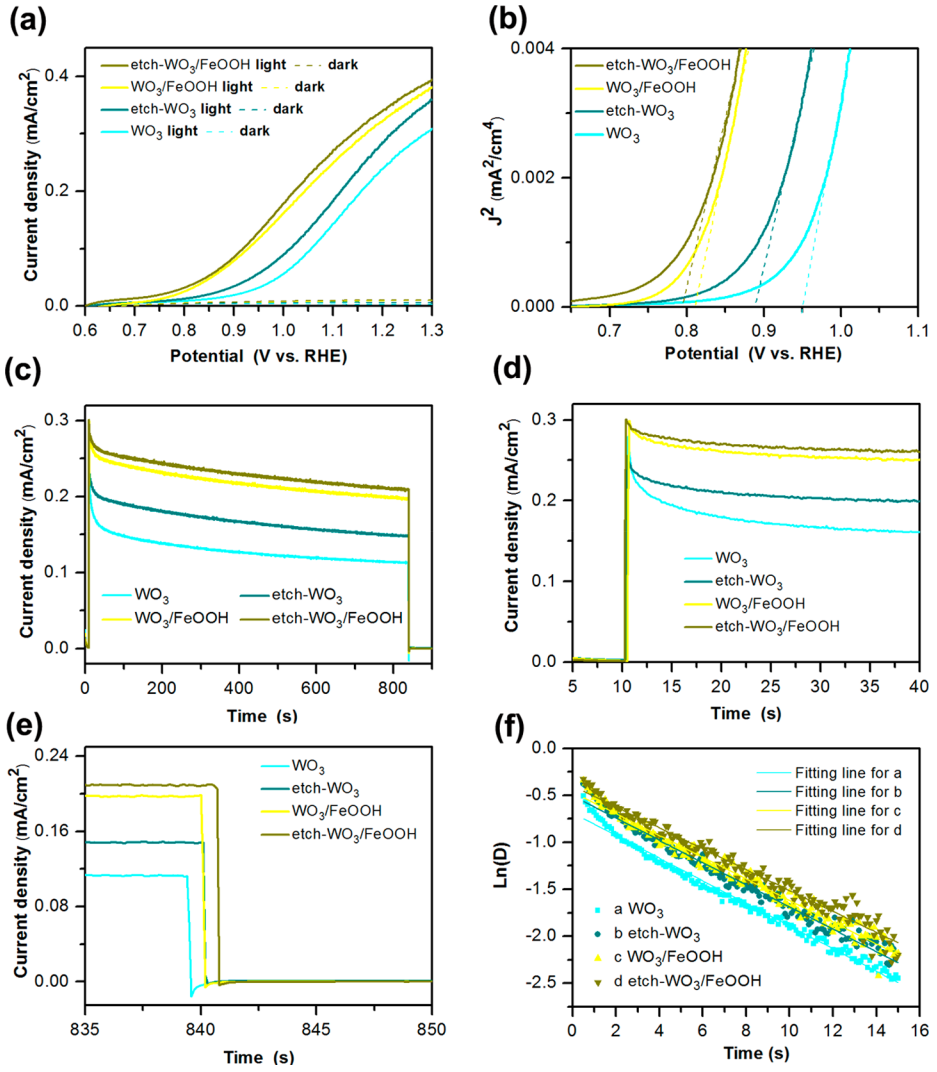

Figure 3. (a) Linear sweep voltammograms and (b) Bulter plots of WO_3, etch-WO_3, WO_3/FeOOH, and etch-WO_3/FeOOH. (c) Current−time curves of WO_3, etch-WO_3, WO_3/FeOOH, and etch-WO_3/FeOOH, (d) magnification at the region of turning on light, (e) magnification at the region of turning off light, and (f) liner fitting for the transient time constant. Each experiment was performed in a 0.2 M Na_2SO_4 solution (pH ≈ 6.8).

elements Ga, O, and W (Figure 2i–k) are evenly distributed on the bulk as shown in the top left corner of the image. The lower right edge of the image, however, shows that it is almost completely composed of Ga without any W (Figure 2h). It indicates that the Ga_2O_3 fabricated by the ALD method covers the entire WO_3 plate.

2.2. Electrochemical Characterization. The effect of etching and electrocatalyst modification on the $J-V$ behavior of the WO_3 photoanode was investigated by linear sweep voltammetry (LSV). For pristine WO_3, the current increases steeply with an increase of the applied potential more positive than 0.9 V vs RHE under illumination (Figures 3a and S10). The corresponding onset potential, extracted by extrapolating the linear part of the Butler plot (J^2-V),[41] is about 0.95 V vs RHE (Figure 3b). For the etch-WO_3 sample, the onset potential shows a negative shift to 0.89 V, and the photocurrent density increases compared with the pristine WO_3 film. Photogenerated holes may accumulate at the surface trapping states (ss) on the surface of the WO_3, where they can recombine with electrons (Figure 4a). This can be alleviated after etching, which reduces the accumulation of photo-

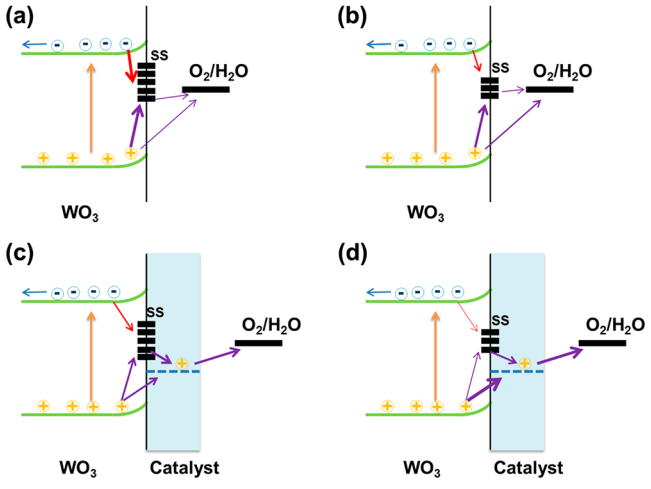

Figure 4. Relative rates of electron−hole recombination and interfacial charge transfer in (a) WO_3, (b) etch-WO_3, (c) WO_3/FeOOH, and (d) etch-WO_3/FeOOH.

DOI: 10.1021/acsami.8b00304
ACS Appl. Mater. Interfaces 2018, 10, 12639−12650

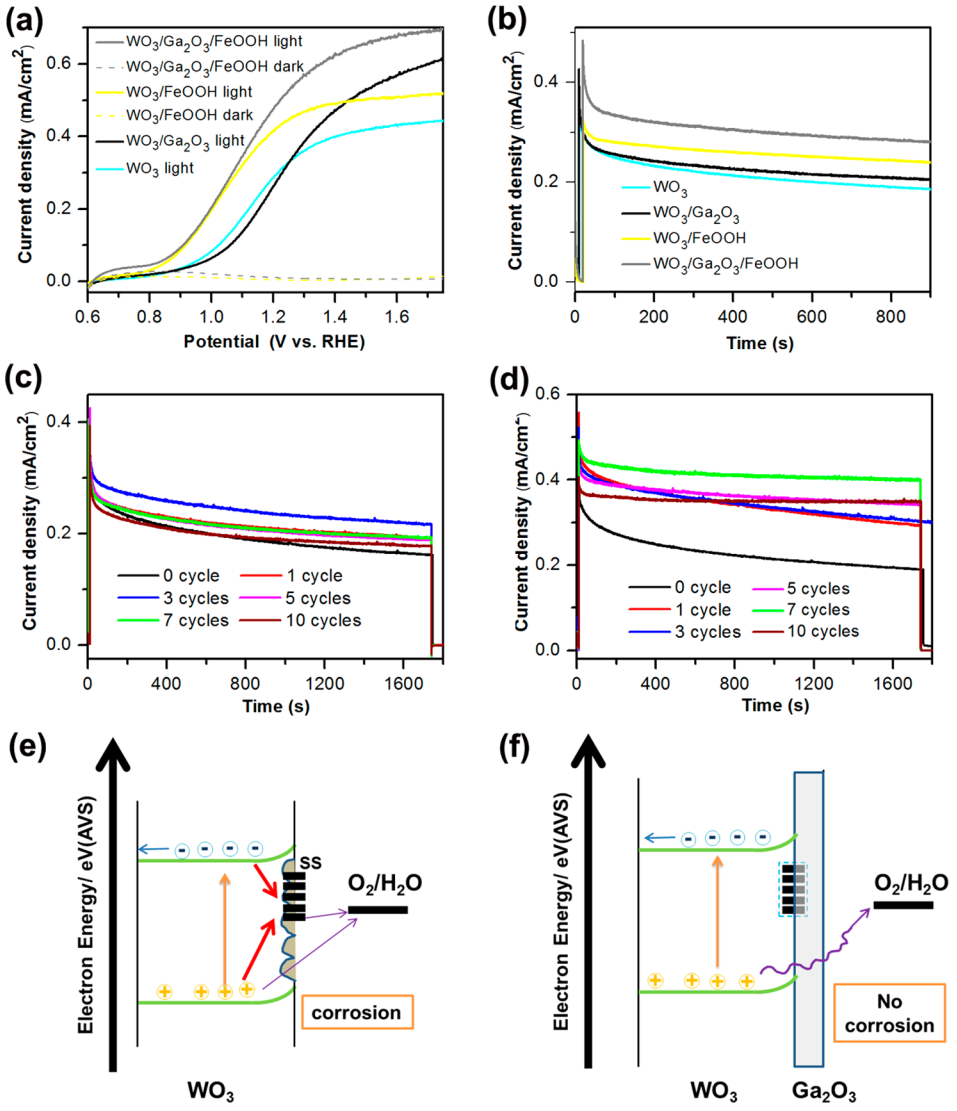

Figure 5. (a) Linear sweep voltammograms. (b) Current−time curves of as-prepared samples at 1.23 V vs RHE and of WO_3 and WO_3/Ga_2O_3 with different ALD cycles under (c) 1.23 and (d) 1.58 V vs RHE. Comparison of WO_3-based photoanode (e) without and (f) with Ga_2O_3 passivation layer. Each experiment was performed in a 0.2 M Na_2SO_4 solution (pH ≈ 6.8).

generated holes by reducing the number of trap sites, allowing more holes to participate in the water oxidation reaction (Figure 4b). The improvement assists in increasing the output photocurrent of the corresponding tandem cells in unassisted water splitting.[42]

After loading FeOOH onto the surface of the pristine WO_3 photoanode, the onset potential shifted negatively to 0.82 V vs RHE (Figure 3b). If the FeOOH is loaded on the surface of the etch-WO_3 sample, the onset potential of etch-WO_3/FeOOH (0.79 V) exhibits a further negative shift as compared to WO_3/FeOOH. FeOOH is hole transfer catalyst, in which the oxidation states of the metal cations cycle during the water oxidation process. Moreover, the rate of electron exchange between the surface traps of the semiconductor and the cations of the catalyst is faster than that of water oxidation (Figure 4c). With the existence of trapping sites on the surface of the WO_3, the photogenerated holes charge the electrocatalyst and surface traps at the same time.[43] After reducing the number of trapping sites, more holes will be available to charge the electrocatalyst (Figure 4d), which can diminish surface state recombination and alleviate Fermi level pinning.[44] The Helmholtz potential at the semiconductor surface may also change with the reduction of surface traps density. This is why the onset potential of WO_3/FeOOH can further negative shift from 0.82 V vs RHE to 0.79 V vs RHE for etch-WO_3/FeOOH (Figure 3b). Meanwhile, the photocurrent increases between 0.8 and 1.3 V vs RHE, indicating a higher fill factor for the etch-WO_3/FeOOH sample.[24] This means a decreased amount of the trap states at the WO_3/FeOOH interface and a more efficient hole transfer from WO_3 to the electrolyte via FeOOH. The CoOOH and dense catalyst (CoO_x) were also used as electrocatalysts to confirm the effect of etching surface traps (Figure S11−15). The further negative shift of onset potential and improvement of photocurrent can also be seen for etch-WO_3/CoO_x and etch-WO_3/CoOOH compared with WO_3/CoO_x and etch-WO_3/CoOOH, respectively. The onset potential of the etch-WO_3/CoO_x shows less negative shift than that of the etch-WO_3/FeOOH (Figure S11a and b), which may cause by different catalytic mechanism between electrolyte-permeated catalyst (FeOOH) and dense electrocatalyst (CoO_x) (Figure S11c and d). In all, the synergistic effect occurs between etching with

DOI: 10.1021/acsami.8b00304
ACS Appl. Mater. Interfaces 2018, 10, 12639−12650

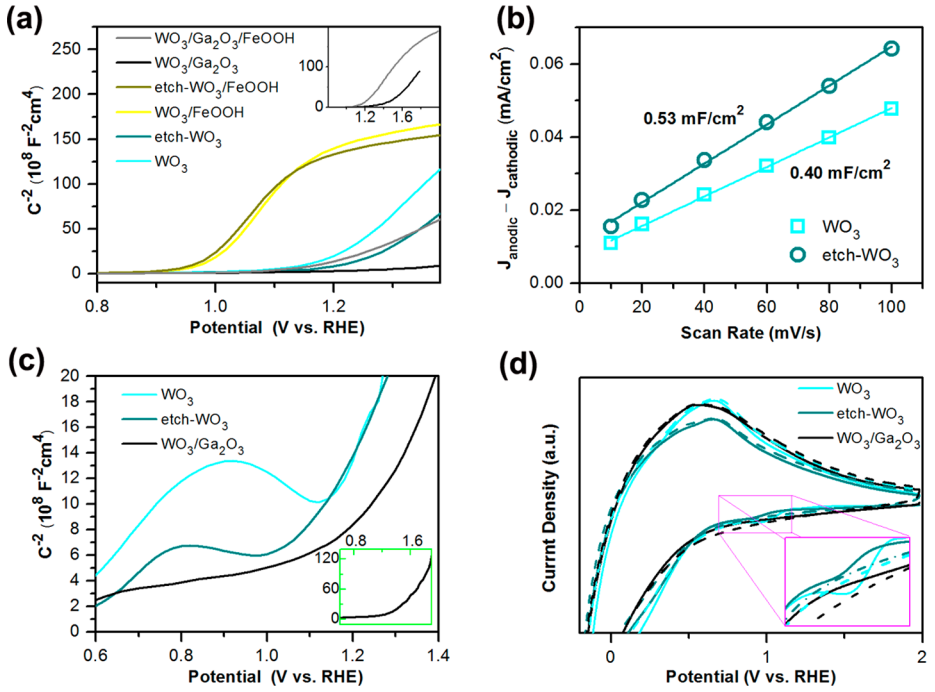

Figure 6. (a) Mott–Schottky plots of samples measured at 1000 Hz, (b) plots used for determination of the double-layer capacitance (C_{dl}) for WO_3 and etch-WO_3, (c) Mott–Schottky plots of samples measured at 5 Hz, and (d) cyclic voltammetry curves measured after current–time test at 2.0 V vs RHE. The inset of panel a is the Mott–Schottky plots of WO_3/Ga_2O_3 and WO_3/Ga_2O_3/FeOOH. The inset of panel c is the Mott–Schottky plots of WO_3/Ga_2O_3. The inset of (d) is the magnification at the potential about 1.0 V vs RHE. Each experiment was performed in a 0.2 M Na_2SO_4 solution (pH ≈ 6.8).

various kind of electrocatalyst, providing a more negative shift of onset potential and a good PEC performance under low-bias.

The current vs time data for all samples was measured at 1.23 V vs RHE for 15 min as shown in Figure 3c. The etch-WO_3 electrode exhibits a slower photocurrent decay curve and a more stable signal than the pristine WO_3 electrode (Figure 3d). Ideally, the photogenerated holes would be transferred to the electrode surface, where they would react with the reduced species of electrolyte, and the photogenerated electrons would move to the back contact. The photocurrent decay demonstrates that holes reaching the electrode surface accumulate at the surface and recombine with electrons from the conduction band rather than transferring to the electrolyte.[45] Additionally, a cathodic spike can be seen for the WO_3 as well as the etch-WO_3 film (Figure 3e), and the latter shows less signal. Taken together, this suggests that trapping sites on the surface of pristine WO_3 accumulate photogenerated holes which then recombine with electrons.[46] After etching, the number of trapping sites has been decreased, and the effect is lessened.

After being modified with FeOOH, etch-WO_3/FeOOH shows a similar initial photocurrent, but a slower decay curve compared with WO_3/FeOOH. The photocurrent decay indicates the recombination of electron–hole pairs, which can be measured and determined from the equations as below (Figure 3f):

$$D = \exp(-t/\tau_{tr}) \quad (1)$$

$$D = (I_t - I_f)/(I_i - I_f) \quad (2)$$

where t is time, τ_{tr} is a parameter defined as the transient time constant. The I_t, I_i, and I_f are the photocurrents at the time after irradiation, initial irradiation, and final steady states, respectively. The calculated average τ_{tr} is 2.6, 4.2, 4.6, and 5.4 s for WO_3, etch-WO_3, WO_3/FeOOH, and etch-WO_3/FeOOH, respectively. The τ_{tr} represents the time needed for the concentration of photogenerated carriers within the WO_3 based film to reach a constant level, and it is related to the rate at which minority carriers (holes) trapped at the surface states capture majority carriers (electrons).[47] The values imply that the etching and subsequent coating of electrocatalysts can mitigate the recombination of photogenerated holes and electrons.

Figure 5a shows the J–V curves of pristine WO_3, WO_3/Ga_2O_3, WO_3/FeOOH, and WO_3/Ga_2O_3/FeOOH. After loading Ga_2O_3, the onset potential of the WO_3 based film electrode shifts to a more positive potential. We also measured WO_3/Ga_2O_3 with different ALD cycles (Figure S16). The photocurrent densities of WO_3/Ga_2O_3 films in the potential region of 0.9–1.2 V vs RHE decrease as the thickness of the passivation layer increases. It indicates that the speed of electrochemical reaction is slower than that of charge transfer in the electrode, resulting in electrochemical polarization as a dominant factor in the process.[36] Moreover, an additional external overpotential may be required to transport holes from the WO_3 to the Ga_2O_3 for efficient water oxidation due to the valence band offset between WO_3 and Ga_2O_3 (Figure S17). At potentials more positive than 1.2 V vs RHE, the photocurrent of the WO_3/Ga_2O_3 film is higher than that of the pristine WO_3. With increasing ALD cycles, the saturated photocurrent densities increase until 7 cycles, as which point they decrease again. This is due to a competition between the beneficial effects of improved passivation and the deleterious effects of decreased carrier tunneling. Meanwhile, charge carriers jumping between defects and penetrating through the layer may be the main source of current.[36]

DOI: 10.1021/acsami.8b00304
ACS Appl. Mater. Interfaces 2018, 10, 12639–12650

After coating with FeOOH (Figure 5a), the onset potentials of the WO_3 and WO_3/Ga_2O_3 films show a negative shift, and there is a negligible difference of onset potential between WO_3/FeOOH and WO_3/Ga_2O_3/FeOOH. The small degree of difference indicates that the outer electrocatalyst layer determines the onset potential, which results from the reduction in the kinetic overpotential. At the same time, the photocurrent of the WO_3/Ga_2O_3/FeOOH film is higher than that of WO_3/FeOOH at 1.23 V vs RHE (Figure 5b). Etch-WO_3 was also loaded of Ga_2O_3 and FeOOH, this sample (etch-WO_3/Ga_2O_3/FeOOH) has similar PEC performance as WO_3/Ga_2O_3/FeOOH (Figure S18). The possible reason for this result is that the recombination of electron−hole pairs has been inhibited via surface trapping sites at the interface between WO_3 and Ga_2O_3. These indicate that the passivation layer suppresses the recombination on the surface of WO_3, leading to a more efficient transfer of photogenerated holes, which suggests that surface passivation strategies can effectively be combined with catalytic approaches.

The current−time data for WO_3/Ga_2O_3 samples with different numbers of ALD cycles was successively measured at 1.23 and 1.58 V vs RHE (Figure 5c and 5d). At each potential, the pristine WO_3 shows a continually decaying photocurrent (Figure S19), which may result from corrosion occurring during the PEC reaction (Figure 5e). WO_3/Ga_2O_3 electrodes exhibit slower decay curves, and the WO_3/Ga_2O_3 sample with ALD cycles of 7 and 10 ALD cycles shows a stable photocurrent after a slight decrease immediately after light-irradiation (Figure 5d). This result shows that the WO_3 sample is prevented from contacting the neutral electrolyte directly, and that chemical corrosion is inhibited (Figure 5f). When the number of ALD cycles is low, the WO_3 plates may not be covered completely due to the existence of pinholes or defects. Increasing the thickness of the Ga_2O_3 layer can not only reduce the pinhole density but also increase the series resistance and build a tunneling barrier.[31] This is why the WO_3/Ga_2O_3 with 10 ALD cycles shows high stability but low photocurrent density. This also explains the fact that the highest photocurrents belong to the WO_3/Ga_2O_3 with 3 and 7 ALD cycles at the potentials of 1.23 and 1.58 V vs RHE, respectively. After irradiation of 1600 s, the photocurrent of the WO_3/Ga_2O_3 with 7 ALD cycles is 0.40 mA/cm^2, about 2 times that of pristine WO_3 (0.19 mA/cm^2). In Figure S20, the etch-WO_3 sample shows higher current density than the pristine WO_3, while the WO_3/Ga_2O_3 exhibits better stability and higher current density (0.73 mA/cm^2) than either the pristine WO_3 (0.34 mA/cm^2) or the etch-WO_3 sample (0.54 mA/cm^2) at 2.0 V (vs RHE). These results demonstrate that Ga_2O_3 deposited by the ALD method has a protective effect on the WO_3 photoanode in a 0.2 M Na_2SO_4 solution (pH ≈ 6.8). Note that there is trade-off relationship between the photocurrent and stability of the WO_3/Ga_2O_3 photoanode, which can be improved by optimizing the number of ALD cycles.

Figure 6a shows the Mott−Schottky plots of WO_3, etch-WO_3, WO_3/FeOOH, etch-WO_3/FeOOH, WO_3/Ga_2O_3, and WO_3/Ga_2O_3/FeOOH film electrodes. Each plot shows a positive slope, distinctly indicating that the WO_3 based films are n-type semiconductors. We also measured the electrochemical active surface area (ECSA) for the WO_3 and etch-WO_3 samples, whose calculated slope is 0.40 and 0.53 mF/cm^2, respectively (Figure 6b). This indicates that etch-WO_3 has a higher ECSA than pristine WO_3.[48,49] The larger specific surface area of the WO_3 electrode may promote charge transfer across the material interfaces (WO_3-electrolyte or WO_3-electrocatalyst). This explains the reason for that the etch-WO_3 film shows positive shifts of flat band potential (E_{fb}) compared to the pristine WO_3 film (Table 1), which is similar to the results for WO_3 etched by PVP and ascorbic acid.[21] The etch-WO_3/FeOOH sample shows slightly higher charge carrier density and a more negative flat band potential than the WO_3/FeOOH sample. These results can be ascribed to the decrease in the number of trapping sites at the interface between WO_3 and FeOOH, which lead to more holes being transferred to the surface of the electrode, in agreement with the results of the current−potential curves (Figure 3a). In comparison to the pristine WO_3 film, the WO_3/Ga_2O_3 films have higher carrier concentrations (1.15×10^{20} /cm^3), which indicates the Ga_2O_3 layer assists in the gathering of charge carriers. The flat band potential of the WO_3/Ga_2O_3 sample is elevated to a more positive potential closer to the valence band in WO_3 than that of pristine WO_3. It continues to shift toward a more positive potential as the thickness of Ga_2O_3 increases monotonically in the dark and under illumination (Figure S20). Hence, Ga_2O_3 acts as a semiconductor passivation layer in this study.[36] After loading of FeOOH, the corresponding flat bands shift to negative potentials when compared with WO_3/Ga_2O_3 (inset of Figure 6a), but they are still more positive than WO_3/FeOOH.

Table 1. Fitting Results of Mott−Schottky plots for WO_3, etch-WO_3, WO_3/FeOOH, etch-WO_3/FeOOH, WO_3/Ga_2O_3, and WO_3/Ga_2O_3/FeOOH Film Electrodes

	WO_3	etch-WO_3	WO_3/FeOOH	etch-WO_3/FeOOH	WO_3/Ga_2O_3	WO_3/Ga_2O_3/FeOOH
carrier density (10^{19}/cm^3)	3.95	4.88	2.81	3.70	11.5	9.79
flat band potential (V vs RHE)	1.10	1.12	0.95	0.91	1.43	1.16

We also measured the Mott−Schottky plots of the WO_3, etch-WO_3, and WO_3/Ga_2O_3 samples with a frequency of 5 Hz (Figure 6c). For pristine WO_3, there is a downward shift in the slope in the potential range of ∼0.9−1.15 V (vs. RHE). Defects may exist on the surface of WO_3, which can lead to Fermi level pinning at the WO_3/electrolyte interface, substantially reduce band bending, and significantly increase charge recombination.[50] Consequently, the upward band bending is suppressed at potentials more negative than 1.15 V (vs RHE), and the photogenerated holes may recombine with photogenerated electrons at undepleted WO_3 surface states before the holes can oxidize water at potentials below 1.15 V (vs RHE). After the etching treatment, a slightly downward shift exists in the plot for the etch-WO_3 sample, indicating that the trapping sites have been dissolved but not completely removed. Further, the downward shift regions shift to more negative potentials, implying that the surface states in the etch-WO_3 sample could be fully depleted at lower potentials than those in pristine WO_3. There is no downward shift in the plot of WO_3/Ga_2O_3. Accordingly, the trapping states of WO_3 might have been completely removed after the loading of Ga_2O_3.

To further study the trapped photogenerated holes on the surface of WO_3, we measured cyclic voltammetry (CV) in the dark (Figure 6d). In this experiment, if holes accumulate on the surface during the current−time curve measurement at 2.0 V vs RHE (Figure S21), a cathodic current peak may be detected in

DOI: 10.1021/acsami.8b00304
ACS Appl. Mater. Interfaces 2018, 10, 12639−12650

the dark when the potential is scanned negatively, which represents the reduction of these surface states.[51] In Figure 6d, the WO_3 sample shows a cathodic peak on the first cycle around 1 V vs RHE, while the peak for etch-WO_3 is much weaker. The peak of each sample is gone on the second CV cycle, meaning that the peak represents the reduction of trapped holes as the potential is scanned negative in the first cycle. For WO_3/Ga_2O_3, the peak can not be observed in the first cycle. This may be explained by a combination of two mechanisms: (1) The photogenerated holes are trapped on the surface of the pristine WO_3, which is restricted after treatment with Ga_2O_3, (2) the formation of peroxo-species may be hampered after coating by the Ga_2O_3 layer. Taking the Mott–Schottky and ECSA results into account, we infer that etching can partially dissolve the trapping sites on the surface, as well as increase the ECSA, which decreases the Fermi pinning. Loading a passivation layer can also efficiently eliminate charge recombination through the surface traps that are assumed to cause Fermi level pinning, which is more completely than etching treatment.

As shown in Figure 7, electrochemical impedance spectra (EIS) studies were carried out to study the properties of the interface between the electrodes and electrolyte solutions. In Figure 7a, both the WO_3 and etch-WO_3 samples show a wide impedance arc without light irradiation, suggesting that few charges can pass through the interface between the photoanode and electrolyte under dark condition.[52] Compared with the WO_3 sample, the etch-WO_3 sample has a smaller impedance arc, which means a small interface transfer resistance that may be caused by the larger ECSA. Under irradiation, the arc diameter of the etch-WO_3 sample is smaller than that of pristine WO_3 (Figure 7b). This indicates that charge transport across the etch-WO_3/electrolyte interface is more facile, consistent with the result from LSV measurements. Meanwhile, the etch-WO_3/FeOOH sample exhibits a smaller impedance arc diameter than the WO_3/FeOOH sample. This implies that the trapping sites that exist at the surface of the pristine WO_3 or the interface between WO_3 and FeOOH are etched and dissolved, which can provide a better charge transfer ability. Following ALD treatment, the WO_3/Ga_2O_3 sample shows larger arc than pristine WO_3 at a low potential (0.88 V vs RHE, Figure 7b), but smaller at a high potential (1.38, 1.48, and 1.58 V vs RHE, Figure 7c). A plausible explanation is that the barrier or internal electric field may exist between WO_3 and Ga_2O_3 after coating of the passivation layer.[36] An additional potential is needed for holes to overcome the barrier at low potential (Figure S17c). In the high potential region, the band alignment facilitates hole transfer to the electrolyte (Figure S17d). Meanwhile, the passivation of surface trapping sites decreases the recombination of electrons and holes, which favors the charge transfer between electrode and electrolyte.

In Figure 8a, it can be seen that the hole injection efficiency for the etch-WO_3 sample increases compared with the pristine WO_3 film, which is consistent with the results of the $J-V$ curves (Figure 3a). The WO_3/FeOOH electrode exhibits higher hole injection efficiency in the low potential region, and etch-WO_3/FeOOH shows even further improvement. In Figure S22a, the photocurrents of the as-prepared samples measured in potassium phosphate (KPi) are consistent with the results measured in 0.2 M Na_2SO_4 (Figure 3a). When measuring the photocurrent in 0.5 M KPi +0.5 M Na_2SO_3 (Figure S22b), the photocurrents of WO_3 and etch-WO_3 are similar, but the photocurrent of etch-WO_3/FeOOH is higher than WO_3/

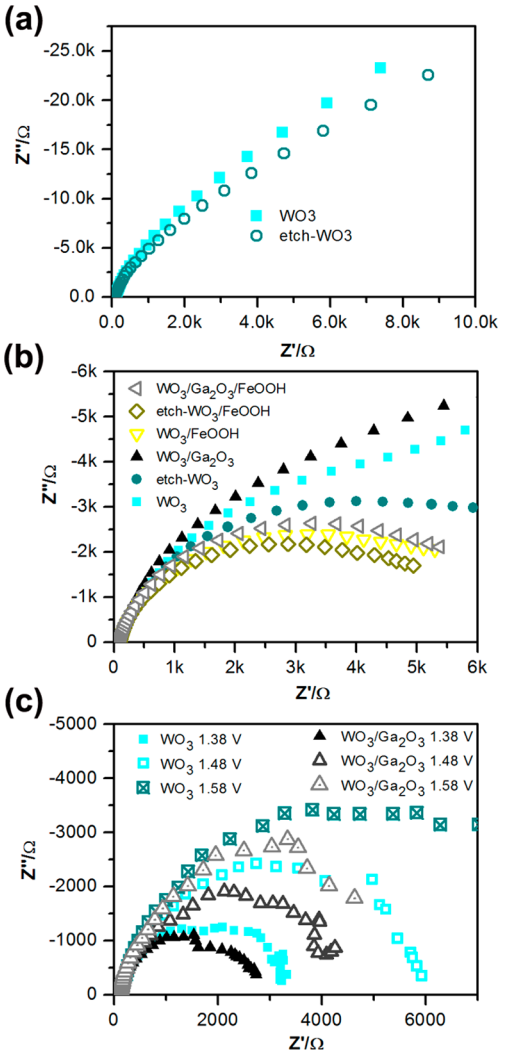

Figure 7. EIS plots: (a) WO_3 and etch-WO_3 in the dark measured at 0.88 V vs RHE; (b) samples under irradiation at 0.88 V vs RHE; (c) WO_3 and WO_3/Ga_2O_3 at different potentials. Each experiment was performed in a 0.2 M Na_2SO_4 solution (pH ≈ 6.8).

FeOOH. This supports the above idea that etching dissolves the trapping sites so as to mitigate the recombination at the interface of WO_3 and electrocatalysts. For WO_3/Ga_2O_3 and WO_3/Ga_2O_3/FeOOH, the efficiencies are lower than WO_3 and WO_3/FeOOH, respectively, in the low potential region. When the applied potential is more positive than 1.0 V vs RHE, the hole injection efficiency of WO_3/Ga_2O_3/FeOOH (96% at 1.23 V vs RHE) is higher than WO_3/FeOOH (77% at 1.23 V vs RHE).

The generated O_2 was also quantified by an oxygen sensor. The Faradaic efficiency of WO_3 is about 80% (Figure 8b), owing to a portion of the total photocurrent going toward the formation of peroxo-species.[32,53,54] After etching, both the amount of evolved oxygen and the Faradaic efficiency increase. A possible explanation is the reduced number of trap states on the surface. WO_3/Ga_2O_3 has a higher efficiency than the etch-WO_3 sample. Besides limiting the trapping sites on the surface of WO_3 from contacting with the electrolyte, the formation of peroxo-species is hampered after coating with the Ga_2O_3 layer, allowing the holes to be used to oxidize H_2O more selectively to O_2. After loading the electrocatalysts, the amount of evolved oxygen and Faradaic efficiency are further improved. The

DOI: 10.1021/acsami.8b00304
ACS Appl. Mater. Interfaces 2018, 10, 12639–12650

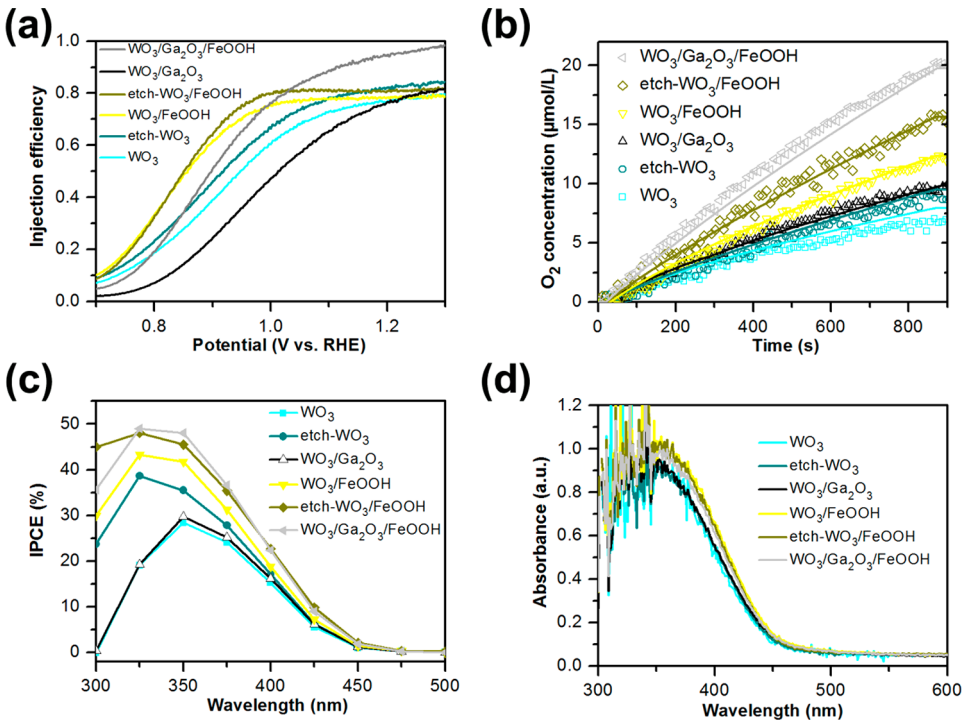

Figure 8. (a) Hole injection efficiency of WO_3-based photoanodes, (b) actual (scatters) and theoretical (line) oxygen evolution amount, (c) incident photon to current conversion efficiency (IPCE) for WO_3 based films (performed at 1.23 V vs RHE in a 0.2 M Na_2SO_4 solution, pH ≈ 6.8), and (d) UV−vis absorbance spectra for WO_3-based films.

Faraday efficiencies are near 100% for WO_3/FeOOH, etch-WO_3/FeOOH, and WO_3/Ga_2O_3/FeOOH. These indicate that the electrocatalyst can promote the photogenerated holes to form O_2 instead of peroxo-species.

Incident photon to current conversion efficiency (IPCE) determinations were performed to further investigate the PEC performances of the samples after surface treatment. In Figure 8c, pristine WO_3 shows a photoresponse in the visible-light region up to about 460 nm. The etch-WO_3 sample exhibits higher IPCE value than the pristine WO_3. The improved IPCE value demonstrates that recombination of photogenerated electrons and holes on the surface of WO_3 is inhibited after etching. After being modified with FeOOH, both the WO_3/FeOOH and etch-WO_3/FeOOH samples show increased IPCE values (Figure 8c). At 350 nm, the IPCE values of WO_3, etch-WO_3, WO_3/FeOOH, and etch-WO_3/FeOOH are approximately 31%, 40%, 43%, and 49%, respectively. It indicates less trapping sites between WO_3 and FeOOH after etching, resulting in a further improvement of PEC performance. Similar results can be seen for the WO_3 modified with dense catalyst (Figure S23a). The IPCE values of etch-WO_3/CoO_x are higher than that of WO_3/CoO_x in the photoresponse region. For WO_3 and WO_3/Ga_2O_3 (Figure S23b), the effect of the passivation layer is significant at a high potential (1.57 V vs RHE), in agreement with the results of the $J-V$ curves (Figure 5a). After being modified with FeOOH (Figure 8c), WO_3/Ga_2O_3/FeOOH shows higher IPCE values than WO_3/FeOOH in the same wavelength region. This demonstrates the synergistic effect of passivation and addition of an electrocatalyst result in a higher PEC performance at 1.23 V (vs Ag/AgCl).

The optical absorption properties of samples were obtained by UV−vis diffused reflectance spectra as indicated in Figure 8d. As can be seen, pristine WO_3 exhibits an intense absorption with an absorption edge at the wavelength near 460 nm, relating to a band gap of 2.70 eV. After etching, there is a negligible shift of the absorbance edge and a minimal change in the absorbance value. For the WO_3/FeOOH and the etch-WO_3/FeOOH samples, the absorbances go up in the ultraviolet region. Similar phenomena can be found for the case of WO_3/CoO_x and etch-WO_3/CoO_x (Figure S25). Moreover, there seems to be a very slight shift in the absorbance edge after loading of CoO_x. Compared with WO_3 and WO_3/FeOOH, WO_3/Ga_2O_3, and WO_3/Ga_2O_3/FeOOH exhibit similar absorbance without changes to the absorbance edge. The corresponding absorbed photon-to-current efficiencies (APCE) are presented in Figure S26. According to the results of IPCE and APCE, we confirm that the improvement of PEC performance results from reducing recombination and increasing hole injection efficiency at the interface of electrode/electrolyte and WO_3/electrocatalyst.

2.3. Electrochemical Characterization of Corresponding Tandem cells. The performance of the WO_3-based film in a solar-powered tandem water-splitting device was measured by connecting the WO_3-based photoanode in series to a DSSC with an additional Pt wire (Figure 9a). The DSSC has higher current density than the photoanode (Figure S27a), and the current curve of the DSSC is almost perpendicular to the x-axis in the current−voltage plot (Figure S27b). Moreover, the $J-V$ curve of the DSSC measured in the tandem cell position (simulated solar irradiation filtered by the WO_3 photoanode) is similar to the DSSC irradiated by the light directly. Therefore, if the onset potential of the photocurrent shifts negatively, the photoanode can get higher photocurrent at the operating potential (U_{op}), where the U_{op} is defined as the potential measured at the intersection of the PV and PEC cell curves. Figure S27b shows the current−voltage curves of the as-prepared electrodes. The difference among photoanodes still

DOI: 10.1021/acsami.8b00304
ACS Appl. Mater. Interfaces 2018, 10, 12639−12650

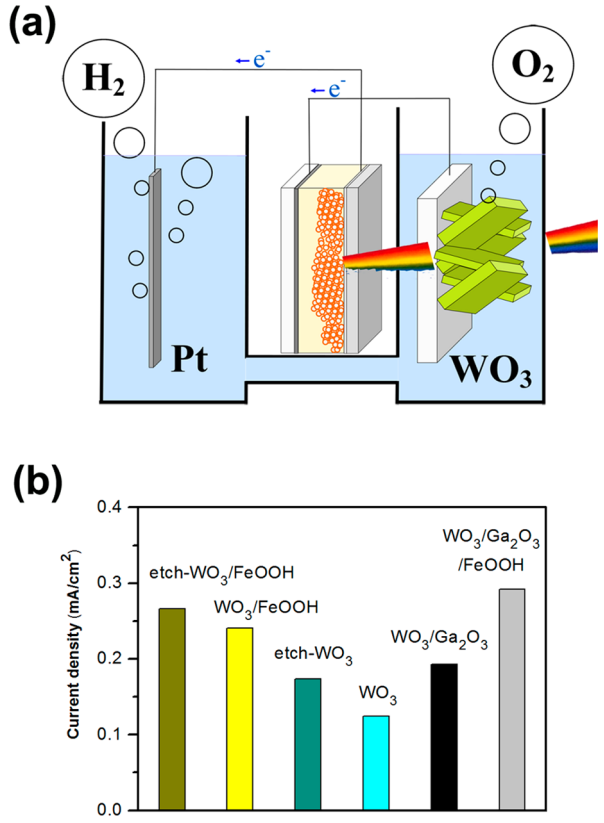

Figure 9. (a) Schematic and (b) output current of tandem cells combined by DSSC- and WO_3-based photoanode

exists in a two-electrode system, which is in agreement with the results of the current−potential curves in a three-electrode system (Figure 3a and 5a). The current density of the WO_3/Ga_2O_3/FeOOH sample is lower than that of WO_3/FeOOH at low voltage, but higher when the external voltage is positive of 0.62 V. The current density at the intersection of different photoanodes with the DSSC follows the trend: WO_3 < WO_3/Ga_2O_3 < etch-WO_3 < WO_3/FeOOH ≤ WO_3/Ga_2O_3/FeOOH < etch-WO_3/FeOOH. Figure S27c presents the photocurrent from the various tandem cells without external voltage. The current densities of the tandem cells are in accordance with the results of LSV, which is WO_3 < etch-WO_3 < WO_3/FeOOH < etch-WO_3/FeOOH. The WO_3/Ga_2O_3 and WO_3/Ga_2O_3/FeOOH show better stability, and the current density of the WO_3/Ga_2O_3/FeOOH sample is higher than that of WO_3/FeOOH and etch-WO_3/FeOOH after irradiation of 20 and 60 s, respectively. After irradiation of 80 s, the output photocurrent of WO_3, etch-WO_3, WO_3/Ga_2O_3, WO_3/FeOOH, etch-WO_3/FeOOH, and WO_3/Ga_2O_3/FeOOH based tandem cell is 0.12, 0.17, 0.19, 0.24, 0.26, and 0.29 mA/cm^2, respectively (Figure 9b). It indicates that output photocurrents were improved to 2.16- and 2.42-fold for etch-WO_3/FeOOH and WO_3/Ga_2O_3/FeOOH based tandem cell compared with the pristine WO_3 based tandem cell.

3. CONCLUSION

In summary, etching, surface passivation, and electrocatalysts have been used to investigate the effect of the interface and surface on the PEC performance of WO_3 based photoanodes and combined tandem cells. Etching can partially dissolve the trapping sites on the surface, as well as increase the ECSA. Loading electrocatalysts can decrease the kinetic overpotential. Both treatments can lower the onset potential. Additionally, after depositing a Ga_2O_3 passivation layer, the WO_3/Ga_2O_3 sample shows a slightly positive shift in the onset potential and higher stability with increasing Ga_2O_3 thickness. An additional catalyst (FeOOH) was loaded on the WO_3/Ga_2O_3 sample to lower the onset potential, and the saturated photocurrent of WO_3/Ga_2O_3/FeOOH is higher than that of WO_3/FeOOH. Both etching and surface passivation treatment decrease the number of trapping sites on the surface of WO_3, which has a synergistic effect with the electrocatalysts on the PEC performance of a WO_3-based electrode. Further, the as-prepared WO_3-based electrodes were combined with a DSSC for fabricating tandem cells. The photoanode with more negative onset potential can exhibit higher photocurrent density in a tandem cell. WO_3/Ga_2O_3/FeOOH shows better stability than WO_3/FeOOH in both single PEC and tandem cells. Taken together, our results clearly indicate that tuning the properties of the interface of the semiconductor/catalyst and semiconductor/electrolyte is of particular importance for solar-powered water oxidation. Meanwhile, it is possible to activate the tandem cell's water splitting capabilities by modifying the surface of the photoelectrode.

■ ASSOCIATED CONTENT

Supporting Information

The Supporting Information is available free of charge on the ACS Publications website at DOI: 10.1021/acsami.8b00304.

Experimental section, XRD patterns, SEM images, EDS mapping, XPS spectra, linear sweep voltammogram curves, current−time curves, schematic energy band diagrams, Mott−Schottky plots, incident photon to current conversion efficiency (IPCE), UV−vis absorbance spectra and absorbed photon-to-current efficiency (APCE) of samples (PDF)

■ AUTHOR INFORMATION

Corresponding Authors

*E-mail: lijieliu@csu.edu.cn.
*E-mail: mullins@che.utexas.edu.

ORCID

Yang Liu: 0000-0002-7240-1546
Jie Lin: 0000-0002-1281-9713
Kenta Kawashima: 0000-0001-7318-6115
Wenzhang Li: 0000-0002-6801-4105
C. Buddie Mullins: 0000-0003-1030-4801

Notes

The authors declare no competing financial interest.

■ ACKNOWLEDGMENTS

The authors acknowledge the generous support of the U.S. National Science Foundation via grant CHE-1664941 and also the Welch Foundation through grant F-1436. Yang Liu thanks Xiaole Chen, Hugo Celio, Karalee Jarvis, Raluca Gearba, Shouliang Zhang, and Edward Evans for the characterization assistance. We also acknowledge the China Scholarship Council (CSC) scholarship under the State Scholarship Fund.

■ REFERENCES

(1) Fujishima, A.; Honda, K. Electrochemical Photolysis of Water at a Semiconductor Electrode. *Nature* **1972**, *238*, 37−38.

DOI: 10.1021/acsami.8b00304
ACS Appl. Mater. Interfaces 2018, 10, 12639−12650

(2) Wang, L.; et al. Electrochemically-Treated $BiVO_4$ Photoanode for Efficient Photoelectrochemical Water Splitting. *Angew. Chem.* **2017**, *129*, 8620−8624.
(3) Schipper, D. E.; Zhao, Z.; Leitner, A. P.; Xie, L.; Qin, F.; Alam, M. K.; Chen, S.; Wang, D.; Ren, Z.; Wang, Z.; Bao, J.; Whitmire, K. H. A TiO_2/Femnp Core/Shell Nanorod Array Photoanode for Efficient Photoelectrochemical Oxygen Evolution. *ACS Nano* **2017**, *11*, 4051−4059.
(4) Elhag, S.; Tordera, D.; Deydier, T.; Lu, J.; Liu, X.; Khranovskyy, V.; Hultman, L.; Willander, M.; Jonsson, M. P.; Nur, O. Low-Temperature Growth of Polyethylene Glycol-Doped $BiZn_2VO_6$ Nanocompounds with Enhanced Photoelectrochemical Properties. *J. Mater. Chem. A* **2017**, *5*, 1112−1119.
(5) Jang, J.-W.; Du, C.; Ye, Y.; Lin, Y.; Yao, X.; Thorne, J.; Liu, E.; McMahon, G.; Zhu, J.; Javey, A.; Guo, J.; Wang, D. Enabling Unassisted Solar Water Splitting by Iron Oxide and Silicon. *Nat. Commun.* **2015**, *6*, 7447.
(6) Brillet, J.; Yum, J.-H.; Cornuz, M.; Hisatomi, T.; Solarska, R.; Augustynski, J.; Graetzel, M.; Sivula, K. Highly Efficient Water Splitting by a Dual-Absorber Tandem Cell. *Nat. Photonics* **2012**, *6*, 824−828.
(7) Shi, X.; Zhang, K.; Shin, K.; Ma, M.; Kwon, J.; Choi, I. T.; Kim, J. K.; Kim, H. K.; Wang, D. H.; Park, J. H. Unassisted Photoelectrochemical Water Splitting Beyond 5.7% Solar-to-Hydrogen Conversion Efficiency by a Wireless Monolithic Photoanode/Dye-Sensitised Solar Cell Tandem Device. *Nano Energy* **2015**, *13*, 182−191.
(8) Butler, M. A. Photoelectrolysis and Physical Properties of the Semiconducting Electrode WO_3. *J. Appl. Phys.* **1977**, *48*, 1914−1920.
(9) Zhao, J.; Olide, E.; Osterloh, F. E. Enhancing Majority Carrier Transport in WO_3 Water Oxidation Photoanode Via Electrochemical Doping. *J. Electrochem. Soc.* **2015**, *162*, H65−H71.
(10) Abdi, F. F.; Han, L.; Smets, A. H. M.; Zeman, M.; Dam, B.; van de Krol, R. Efficient Solar Water Splitting by Enhanced Charge Separation in a Bismuth Vanadate-Silicon Tandem Photoelectrode. *Nat. Commun.* **2013**, *4*, 2195.
(11) Kosar, S.; Pihosh, Y.; Turkevych, I.; Mawatari, K.; Uemura, J.; Kazoe, Y.; Makita, K.; Sugaya, T.; Matsui, T.; Fujita, D.; Tosa, M.; Struk, Y. M.; Kondo, M.; Kitamori, T. Tandem Photovoltaic−Photoelectrochemical Gaas/Ingaasp−WO_3/$BiVO_4$ Device for Solar Hydrogen Generation. *Jpn. J. Appl. Phys.* **2016**, *55*, 04ES01.
(12) Shinde, A.; Guevarra, D.; Liu, G.; Sharp, I. D.; Toma, F. M.; Gregoire, J. M.; Haber, J. A. Discovery of Fe-Ce Oxide/$BiVO_4$ Photoanodes through Combinatorial Exploration of Ni-Fe-Co-Ce Oxide Coatings. *ACS Appl. Mater. Interfaces* **2016**, *8*, 23696−23705.
(13) Han, J.; Zong, X.; Wang, Z.; Li, C. A Hematite Photoanode with Gradient Structure Shows an Unprecedentedly Low Onset Potential for Photoelectrochemical Water Oxidation. *Phys. Chem. Chem. Phys.* **2014**, *16*, 23544−23548.
(14) Malara, F.; Fabbri, F.; Marelli, M.; Naldoni, A. Controlling the Surface Energetics and Kinetics of Hematite Photoanodes through Few Atomic Layers of NiO_x. *ACS Catal.* **2016**, *6*, 3619−3628.
(15) Pham, T. A.; Ping, Y.; Galli, G. Modelling Heterogeneous Interfaces for Solar Water Splitting. *Nat. Mater.* **2017**, *16*, 401−408.
(16) Klahr, B.; Gimenez, S.; Fabregat-Santiago, F.; Hamann, T.; Bisquert, J. Water Oxidation at Hematite Photoelectrodes: The Role of Surface States. *J. Am. Chem. Soc.* **2012**, *134*, 4294−4302.
(17) Le Formal, F.; Pendlebury, S. R.; Cornuz, M.; Tilley, S. D.; Grätzel, M.; Durrant, J. R. Back Electron−Hole Recombination in Hematite Photoanodes for Water Splitting. *J. Am. Chem. Soc.* **2014**, *136*, 2564−2574.
(18) Kafi, F. S. B.; Jayathileka, K. M. D. C.; Wijesundera, R. P.; Siripala, W. Fermi-Level Pinning and Effect of Deposition Bath PH on the Flat-Band Potential of Electrodeposited N-Cu_2O in an Aqueous Electrolyte. Phys. *Phys. Status Solidi B* **2016**, *253*, 1965−1969.
(19) Caccamo, L.; Fàbrega, C.; Marschewski, M.; Fündling, S.; Gad, A.; Casals, O.; Lilienkamp, G.; Höfft, O.; Prades, J. D.; Daum, W.; Waag, A. Charge Transfer Characteristics of n-Type $In_{0.1}Ga_{0.9}N$ Photoanode across Semiconductor−Liquid Interface. *J. Phys. Chem. C* **2016**, *120*, 28917−28923.
(20) Cho, I. S.; Han, H. S.; Logar, M.; Park, J.; Zheng, X. Enhancing Low-Bias Performance of Hematite Photoanodes for Solar Water Splitting by Simultaneous Reduction of Bulk, Interface, and Surface Recombination Pathways. *Adv. Energy Mater.* **2016**, *6*, 1501840.
(21) Li, W.; Da, P.; Zhang, Y.; Wang, Y.; Lin, X.; Gong, X.; Zheng, G. WO_3 Nanoflakes for Enhanced Photoelectrochemical Conversion. *ACS Nano* **2014**, *8*, 11770−11777.
(22) Zhao, Z.; Butburee, T.; Lyv, M.; Peerakiatkhajohn, P.; Wang, S.; Wang, L.; Zheng, h. Etching Treatment of Vertical WO_3 Nanoplates as Photoanode for Enhanced Photoelectrochemical Performance. *RSC Adv.* **2016**, *6*, 68204−68210.
(23) Liu, R.; Zheng, Z.; Spurgeon, J.; Yang, X. Enhanced Photoelectrochemical Water-Splitting Performance of Semiconductors by Surface Passivation Layers. *Energy Environ. Sci.* **2014**, *7*, 2504−2517.
(24) Ding, C.; Shi, J.; Wang, Z.; Li, C. Photoelectrocatalytic Water Splitting: Significance of Cocatalysts, Electrolyte and Interfaces. *ACS Catal.* **2017**, *7*, 675−688.
(25) Seabold, J. A.; Choi, K.-S. Effect of a Cobalt-Based Oxygen Evolution Catalyst on the Stability and the Selectivity of Photo-Oxidation Reactions of a WO_3 Photoanode. *Chem. Mater.* **2011**, *23*, 1105−1112.
(26) Cristino, V.; Berardi, S.; Caramori, S.; Argazzi, R.; Carli, S.; Meda, L.; Tacca, A.; Bignozzi, C. A. Efficient Solar Water Oxidation Using Photovoltaic Devices Functionalized with Earth-Abundant Oxygen Evolving Catalysts. *Phys. Chem. Chem. Phys.* **2013**, *15*, 13083−13092.
(27) Huang, J.; Ding, Y.; Luo, X.; Feng, Y. Solvation Effect Promoted Formation of P−N Junction between WO_3 and FeOOH: A High Performance Photoanode for Water Oxidation. *J. Catal.* **2016**, *333*, 200−206.
(28) Dalle Carbonare, N.; Cristino, V.; Berardi, S.; Carli, S.; Argazzi, R.; Caramori, S.; Meda, L.; Tacca, A.; Bignozzi, C. A. Hematite Photoanodes Modified with an Feiii Water Oxidation Catalyst. *ChemPhysChem* **2014**, *15*, 1164−1174.
(29) Lhermitte, C. R.; Garret Verwer, J.; Bartlett, B. M. Improving the Stability and Selectivity for the Oxygen-Evolution Reaction on Semiconducting WO_3 Photoelectrodes with a Solid-State FeOOH Catalyst. *J. Mater. Chem. A* **2016**, *4*, 2960−2968.
(30) Sivula, K. Metal Oxide Photoelectrodes for Solar Fuel Production, Surface Traps, and Catalysis. *J. Phys. Chem. Lett.* **2013**, *4*, 1624−1633.
(31) Bae, D.; Seger, B.; Vesborg, P. C. K.; Hansen, O.; Chorkendorff, I. Strategies for Stable Water Splitting Via Protected Photoelectrodes. *Chem. Soc. Rev.* **2017**, *46*, 1933−1954.
(32) Hill, J. C.; Choi, K.-S. Effect of Electrolytes on the Selectivity and Stability of n-Type WO_3 Photoelectrodes for Use in Solar Water Oxidation. *J. Phys. Chem. C* **2012**, *116*, 7612−7620.
(33) Wang, G.; Ling, Y.; Wang, H.; Yang, X.; Wang, C.; Zhang, J. Z.; Li, Y. Hydrogen-Treated WO_3 Nanoflakes Show Enhanced Photostability. *Energy Environ. Sci.* **2012**, *5*, 6180−6187.
(34) Kim, W.; Tachikawa, T.; Monllor-Satoca, D.; Kim, H.-i.; Majima, T.; Choi, W. Promoting Water Photooxidation on Transparent WO_3 Thin Films Using an Alumina Overlayer. *Energy Environ. Sci.* **2013**, *6*, 3732−3739.
(35) Le Formal, F.; Tetreault, N.; Cornuz, M.; Moehl, T.; Gratzel, M.; Sivula, K. Passivating Surface States on Water Splitting Hematite Photoanodes with Alumina Overlayers. *Chem. Sci.* **2011**, *2*, 737−743.
(36) Xing, Z.; Ren, F.; Wu, H.; Wu, L.; Wang, X.; Wang, J.; Wan, D.; Zhang, G.; Jiang, C. Enhanced PEC Performance of Nanoporous Si Photoelectrodes by Covering HfO_2 and TiO_2 Passivation Layers. *Sci. Rep.* **2017**, *7*, 43901.
(37) Yang, Y.; Xie, R.; Liu, Y.; Li, J.; Li, W. Effect of Surface Passivation on Photoelectrochemical Water Splitting Performance of WO_3 Vertical Plate-Like Films. *Catalysts* **2015**, *5*, 2024−2038.
(38) Liu, Y.; Li, J.; Li, W.; Liu, Q.; Yang, Y.; Li, Y.; Chen, Q. Enhanced Photoelectrochemical Performance of WO_3 Film with HfO_2 Passivation Layer. *Int. J. Hydrogen Energy* **2015**, *40*, 8856−8863.

DOI: 10.1021/acsami.8b00304
ACS Appl. Mater. Interfaces 2018, 10, 12639−12650

(39) Zeng, Q.; Li, J.; Bai, J.; Li, X.; Xia, L.; Zhou, B. Preparation of Vertically Aligned WO_3 Nanoplate Array Films Based on Peroxotungstate Reduction Reaction and Their Excellent Photoelectrocatalytic Performance. *Appl. Catal., B* **2017**, *202*, 388−396.
(40) Wang, L.; Yang, Y.; zhang, y.; Rui, Q.; Zhang, B.; Shen, Z.; Bi, Y. One Dimensional Hematite Photoanodes with Spatially Separated Pt and FeOOH Nanolayers for Efficient Solar Water Splitting. *J. Mater. Chem. A* **2017**, *5*, 17056−17063.
(41) Xiao, J.; Huang, H.; Huang, Q.; Li, X.; Hou, X.; Zhao, L.; Ma, R.; Chen, H.; Li, Y. Remarkable Improvement of the Turn−on Characteristics of a Fe_2O_3 Photoanode for Photoelectrochemical Water Splitting with Coating a FeCoW Oxy−Hydroxide Gel. *Appl. Catal., B* **2017**, *212*, 89−96.
(42) Steier, L.; Herraiz-Cardona, I.; Gimenez, S.; Fabregat-Santiago, F.; Bisquert, J.; Tilley, S. D.; Grätzel, M. Understanding the Role of Underlayers and Overlayers in Thin Film Hematite Photoanodes. *Adv. Funct. Mater.* **2014**, *24*, 7681−7688.
(43) Nellist, M. R.; Laskowski, F. A. L.; Lin, F.; Mills, T. J.; Boettcher, S. W. Semiconductor−Electrocatalyst Interfaces: Theory, Experiment, and Applications in Photoelectrochemical Water Splitting. *Acc. Chem. Res.* **2016**, *49*, 733−740.
(44) Zandi, O.; Hamann, T. W. Enhanced Water Splitting Efficiency through Selective Surface State Removal. *J. Phys. Chem. Lett.* **2014**, *5*, 1522−1526.
(45) Hagfeldt, A.; Lindström, H.; Södergren, S.; Lindquist, S.-E. Photoelectrochemical Studies of Colloidal TiO_2 Films: The Effect of Oxygen Studied by Photocurrent Transients. *J. Electroanal. Chem.* **1995**, *381*, 39−46.
(46) Gao, Y.; Hamann, T. W. Elucidation of $CuWO_4$ Surface States During Photoelectrochemical Water Oxidation. *J. Phys. Chem. Lett.* **2017**, *8*, 2700−2704.
(47) Radecka, M.; Wnuk, A.; Trenczek-Zajac, A.; Schneider, K.; Zakrzewska, K. TiO_2/SnO_2 Nanotubes for Hydrogen Generation by Photoelectrochemical Water Splitting. *Int. J. Hydrogen Energy* **2015**, *40*, 841−851.
(48) Wu, Y.; Li, G.-D.; Liu, Y.; Yang, L.; Lian, X.; Asefa, T.; Zou, X. Overall Water Splitting Catalyzed Efficiently by an Ultrathin Nanosheet-Built, Hollow Ni_3S_2-Based Electrocatalyst. *Adv. Funct. Mater.* **2016**, *26*, 4839−4847.
(49) Feng, X.; Chen, Y.; Qin, Z.; Wang, M.; Guo, L. Facile Fabrication of Sandwich Structured WO_3 Nanoplate Arrays for Efficient Photoelectrochemical Water Splitting. *ACS Appl. Mater. Interfaces* **2016**, *8*, 18089−18096.
(50) Zhong, M.; Hisatomi, T.; Sasaki, Y.; Suzuki, S.; Teshima, K.; Nakabayashi, M.; Shibata, N.; Nishiyama, H.; Katayama, M.; Yamada, T.; Domen, K. Highly Active Gan-Stabilized Ta_3N_5 Thin-Film Photoanode for Solar Water Oxidation. *Angew. Chem., Int. Ed.* **2017**, *56*, 4739−4743.
(51) Klahr, B.; Gimenez, S.; Fabregat-Santiago, F.; Bisquert, J.; Hamann, T. W. Electrochemical and Photoelectrochemical Investigation of Water Oxidation with Hematite Electrodes. *Energy Environ. Sci.* **2012**, *5*, 7626−7636.
(52) Zheng, J. Y.; Song, G.; Hong, J.; Van, T. K.; Pawar, A. U.; Kim, D. Y.; Kim, C. W.; Haider, Z.; Kang, Y. S. Facile Fabrication of WO_3 Nanoplates Thin Films with Dominant Crystal Facet of (002) for Water Splitting. *Cryst. Growth Des.* **2014**, *14*, 6057−6066.
(53) Park, M.; Seo, J. H.; Song, H.; Nam, K. M. Enhanced Visible Light Activity of Single-Crystalline WO_3 Microplates for Photoelectrochemical Water Oxidation. *J. Phys. Chem. C* **2016**, *120*, 9192−9199.
(54) Mi, Q.; Coridan, R. H.; Brunschwig, B. S.; Gray, H. B.; Lewis, N. S. Photoelectrochemical Oxidation of Anions by WO_3 in Aqueous and Nonaqueous Electrolytes. *Energy Environ. Sci.* **2013**, *6*, 2646−2653.

DOI: 10.1021/acsami.8b00304
ACS Appl. Mater. Interfaces 2018, 10, 12639−12650